Journal of Applied Fluid Mechanics, Vol. 18, No. 12, pp. 3116-3131, 2025.
Available online at www.jafmonline.net, ISSN 1735-3572, EISSN 1735-3645.
https://doi.org/10.47176/jafm.18.12.3380

Performance Optimization of Fuel Cell Vehicle Air Compressor Impeller Based on Multi-objective Whale Optimization Algorithm

Y. Sun[1], H. Yin[1, 2†], W. Song[3], X. Sun[1], A. Li[1] and Y. Chen[1]

[1] *School of transportation and vehicle engineering, Shandong University of Technology, Zibo 255022, China*
[2] *Shandong Key Laboratory of Integrated Design and Intelligence of New Energy Vehicles, Zibo, 55022, China*
[3] *Wuxi Weitongli New Energy Electric Co., Ltd., Wuxi 214000, China*

†*Corresponding Author Email: yinhongbin@sdut.edu.cn*

ABSTRACT

As fuel cell vehicles have broad development prospects, improving the performance of their air compressors is crucial for the normal and efficient operation of onboard fuel cells. To improve the performance of the air compressor and solve the contradictory relationship between the pressurization capability and efficiency of the impeller, this study proposes a method combining an approximation model and a multi-objective whale optimization algorithm. First, three-dimensional numerical models of the single-flow passage and the full compressor flow passage in the impeller were established, and the accuracy of the numerical calculations was verified using open-test-case compressors. Then, choosing the pressure ratio and isentropic efficiency as the optimization objectives, sensitivity analysis of the structural parameters of the impeller was conducted via Latin hypercube sampling, and surrogate optimization models were constructed using the least squares method for designing and setting the typical operating conditions for the impeller. Finally, the whale optimization algorithm, which is superior in impeller optimization compared to genetic algorithms, was employed to derive the Pareto solution set. Compared to the original impeller, the optimized impeller exhibited improvements in the pressure ratio as well as isentropic efficiency for the single-flow passage as well as full-model configurations. Under design conditions, the pressure ratio and isentropic efficiency increased by 5.5 % and 1.4 %, respectively, whereas under typical operating conditions, they improved by 3.6 % and 4.1 %, respectively. In addition, the three-dimensional flow characteristic analysis revealed reductions in the internal losses and recirculation within the optimized impeller. Thus, we can conclude that the proposed optimization method effectively enhances the overall performance of the fuel cell vehicle compressors.

Article History

Received February 17, 2025
Revised June 25, 2025
Accepted July 4, 2025
Available online October 6, 2025

Keywords:

Fuel cell vehicle
Centrifugal compressor
Aerodynamic performance
Flow field simulation
Multi-objective optimization

1. INTRODUCTION

With the advancement of global industrialization and the continuous increase in vehicle ownership, persistent consumption of fossil fuels has caused severe environmental pollution and resource depletion (Boroujerdi et al., 2025; Abdullah et al., 2024). To resolve the conflict between automotive industry development and sustainable development, different countries are actively researching new energy vehicles (Abedin et al., 2025). Proton-exchange membrane fuel cells (PEMFC), which have gained prominence due to their pollution-free operation, zero emissions, and high efficiency, are evaluated as one of the most promising zero-emission new energy vehicles. (Manzo et al., 2025). As one of the critical components of PEMFCs systems, besides the stack, the performance of the air compressors directly affects the efficiency of the power system. However, the current centrifugal compressors consume excessive power, comprising 15-25% of the stack's total power generation, and their performance significantly affects the efficiency of the PEMFCs (Chen et al., 2023). Therefore, high-performance and high-efficiency centrifugal compressors are crucial for ensuring a sustained and efficient operation of PEMFCs.

The impeller, as the sole energy-converting component in a compressor, operates at extremely high rotational speeds to convert kinetic energy into static

NOMENCLATURE

PEMFC	Proton Exchange Membrane Fuel Cell	ρ	density
CFD	Computational Fluid Dynamics	i , j	tensor symbols
LHS	Latin Hypercube Sampling	κ	turbulence kinetic energy
WOA	Whale Optimization Algorithm	t	time of fluid flow
SST	Shear Stress Transport	λ	air chemical stoichiometry
MRF	Multiple Reference Frame	P_e	stack power
NSGA-II	Non-Dominated Sorting Genetic Algorithm II	V_c	average cell voltage of the stack
NAWOA	Non-Dominated Sorting Whale Optimization Algorithm	D_2	impeller outlet diameter
COWA	Continuous Ordered Weighted Averaging	D_1	impeller inlet diameter
B2B	Blade-to-blade	D_h	hub diameter
β_{2A}	outlet blade angle	b_1	outlet width
β_{1A}	inlet blade angle	Z	number of blades
$P1t$	inlet static pressure	k	adiabatic index of air
P_{2t}	outlet static pressure	T_1	inlet total temperature
ε	pressure ratio	T_2	outlet total temperature
P_1	inlet total pressure	P_2	outlet total pressure
Pr	pressure ratio	Ie	isentropic efficiency

pressure energy. Suboptimal or optimized designs of the structural and geometric parameters, and the blade angles and profiles of the impeller profoundly influence its pressure ratio as well as efficiency. This issue is not unique to compressors but also exists in centrifugal pumps and similar machinery (Al-Obaidi, 2023). Consequently, extensive scholarly efforts have focused on impeller aerodynamic design and computational optimization.

Ekradi and Madadi (2020) proposed an optimization method combining a 3D blade parameterization approach, genetic algorithms, artificial neural networks, and computational fluid dynamics. This method optimized 28 control points that determined the blade geometry, including the blade angle variables, significantly improving the efficiency of the compressor. However, the non-design conditions were not considered. Hong et al. (2022) used the critical point theory and probabilistic definitions to study the structural parameters of the impeller in fuel-cell air compressors. Their analysis revealed that the tip clearance, hub, and horseshoe vortices were critical factors that influenced the aerodynamic performance of the impeller, resulting in a 1.47 % improvement in pressure ratio of the compressor. A Turkish scholar (Soylemez et al., 2024) applied genetic algorithms to optimize the structural parameters of the impeller and explored their impact on the isentropic efficiency and pressure ratio limits. Numerical results under different flow rates were compared with the experimental data, showing the maximum and minimum errors are 1.98% and 0.35% respectively, providing valuable insights for designing advanced tandem blade compressors. Zhang et al. (2024) investigated the effect of the inlet tip clearance on the performance of the compressor, revealing the mechanism of the tip leakage flow. Using fast Fourier transform spectral analysis, they concluded that reducing the inlet tip clearance effectively extended the operating range of the air compressor and enhanced its aerodynamic performance. Anbarsooz et al. (2024) studied the influence of the diffuser blade wrap angle and blade count on the centrifugal compressor performance. Their findings indicated that increasing the wrap angle enhanced the throttling flow, but reduced the pressure ratio at low flow rates, whereas the blade count significantly affected the operating range and pressure ratio of the compressor. Ma et al. (2021) trained a data-driven surrogate model based on support vector machines and integrated it with the nondominated sorting genetic algorithm (NSGA-III) to identify the optimal solutions for structural optimization problems. Guo et al. (2014) employed a second-order response method for the geometric optimization of small centrifugal compressors, achieving a 7.5 % increase in their pressure ratio. Sun et al. (2024) utilized computational fluid dynamics and a stacked model to optimize the structural parameters of a compressor using a multi-objective random walk grey wolf optimizer algorithm. Based on the 3D flow analysis, the study demonstrated the parameter effects on performance improvement, resulting in enhancements of 2.8 % in the pressure ratio, 2.3 % in the outlet temperature, 9.3 % in the isentropic efficiency, and 16.0 % in the adiabatic compression work. Chen et al. (2023) adopted a one-dimensional approach and developed a multidisciplinary design optimization method that combined empirical one-dimensional loss models, statistical analysis, and multiple optimization theories. Using the signal-to-noise ratio variance analysis and multi-objective optimization based on the grey relational grade, the study identified the impeller exit width and radius are the key that affect the performance of the air compressor. This approach reduced the power loss by 2.99 % and improves the isentropic efficiency by 1.24 %. Furthermore, optimization design of impellers has also been demonstrated to enhance pump performance (Al-Obaidi & Alhamid, 2024; Al-Obaidi, 2024). By analyzing the distributions of velocity, turbulent kinetic energy, and pressure, studies on the flow characteristics and dynamics of axial-flow pumps can provide references for internal flow research in compressors (Al-Obaidi & Alhamid 2025; Al-Obaidi et al., 2023), providing detailed and in-depth references for this study.

In summary, impeller optimization can significantly enhance the pressure ratio and isentropic efficiency of

centrifugal compressors. However, as the aforementioned research indicates, very few studies have investigated and optimized the combined design conditions and the common operating conditions of fuel cell air compressors. The designing of the impeller remains a complex process. Traditional empirical optimization methods rely heavily on individual experience, resulting in high labor costs. Concurrently, the current impeller optimization process predominantly employs single-objective approaches or uses weighted coefficients to consolidate multiple objectives into a single target, which risks local optima. Furthermore, fuel cell vehicle operation involves variable conditions, a large number of studies only consider the optimization of design conditions, while ignoring the common operating conditions. Thus, in addition to adopting surrogate models for reducing the simulation costs and improving the optimization efficiency of the compressors, it is essential to perform multi-objective optimization across diverse operating conditions to enhance their practical applicability and accuracy. This study integrates computational fluid dynamics (CFD) methods, Latin hypercube sampling (LHS), surrogate models, and the whale optimization algorithm (WOA) to achieve multi-objective optimization of the structural parameters of the impeller. This study contributes in the following ways:

(1) CFD single-flow passage and full-stage compressor models were established for fuel cell vehicle compressors.

(2) A sensitivity analysis of the impeller structural parameters was conducted via LHS.

(3) Surrogate models were constructed for the design and typical operating conditions using the least-squares method.

(4) An enhanced WOA was implemented for multi-objective optimization, followed by a comparative analysis of the flow characteristics between the baseline and optimized impellers.

2. NUMERICAL CALCULATIONS

2.1 Numerical Methodology

The equation of continuity (Munson et al., 2013) is written as:

$$\frac{\partial \rho}{\partial t}+\frac{\partial(\rho u)}{\partial x}+\frac{\partial(\rho v)}{\partial y}+\frac{\partial(\rho w)}{\partial z}=0 \tag{1}$$

The equation of momentum is (Munson et al., 2013):

$$\frac{\partial(\rho u_i)}{\partial t}+\frac{\partial(\rho u_i u_j)}{\partial x_i}=S_i-\frac{\partial \rho}{x_i}+\frac{\partial}{x_i}(\mu\frac{\partial u_i}{\partial x_i}-\rho\overline{u}_i\overline{u}_j) \tag{2}$$

The equation of total energy is (Munson et al., 2013):

$$\frac{\partial(\rho h_{tot})}{\partial t}-\frac{\partial \rho}{\partial t}+\nabla(\rho U h_{tot})=S_E+\nabla(U\tau)+US_M+\nabla(\lambda\nabla T) \tag{3}$$

where h_{tot} symbolizes the total enthalpy is:

$$h_{tot}=h+\frac{1}{2}U^2 \tag{4}$$

In the numerical simulations of centrifugal compressors, the widely adopted turbulence model is the shear stress transport (SST) model. It integrates the strengths of both the k-epsilon (k-ε) model as well as the k-omega (k-ω) model (Niveditha et al., 2023). Numerous studies have employed the SST turbulence model, which has been extensively used in compressor flow simulations and has demonstrated high accuracy (Al-Obaidi, 2024b; Li et al., 2025; Al-Obaidi et al., 2024).

The equation of the turbulence kinetic energy, κ, (Zhang et al., 2024) is:

$$\frac{\partial(\rho k)}{\partial t}+\frac{\partial(\rho k u_j)}{\partial x_j}=\frac{\partial}{\partial x_j}\left[\left(\mu+\frac{\mu_t}{\sigma_k}\right)\frac{\partial k}{\partial x_j}\right]+G_k-Y_k+S_k \tag{5}$$

The equation of the turbulence dissipation rate, ω, (Zhang et al., 2024) is:

$$\frac{\partial(\rho\omega)}{\partial t}+\frac{\partial(\rho\omega u_i)}{\partial x_i}=\frac{\partial}{\partial x_j}\left[\left(\mu+\frac{\mu_t}{\sigma_k}\right)\frac{\partial \omega}{\partial x_j}\right]+G_\omega-Y_\omega+D_\omega+S_\omega \tag{6}$$

2.2 Model of Centrifugal Compressor

The compressor serves as the central unit within the oxygen supply architecture of PEMFCs. Maintaining an appropriate supply pressure is critical for the system performance as well as cost optimization. As shown in Fig. 1, increasing the supply pressure enhances the power density while indirectly reducing the manufacturing costs. Therefore, this study adopted a pressure ratio of 2.2, which satisfies the power density requirements of the system while demonstrating cost-effectiveness (Yu et al., 2015; Wu et al., 2023).

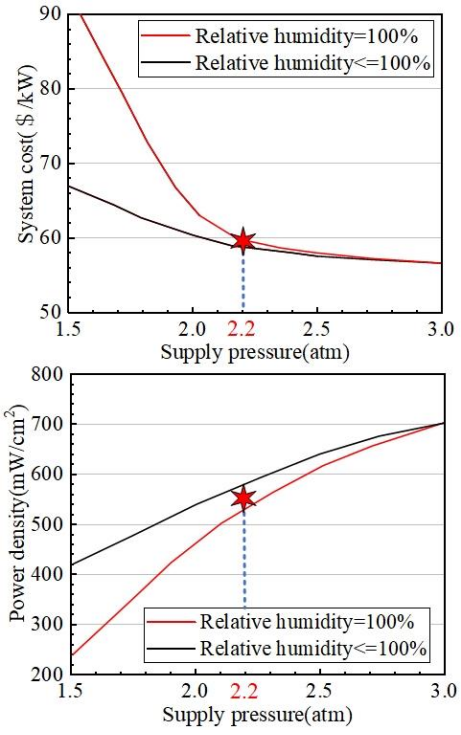

Fig. 1 System cost analysis of fuel cell system

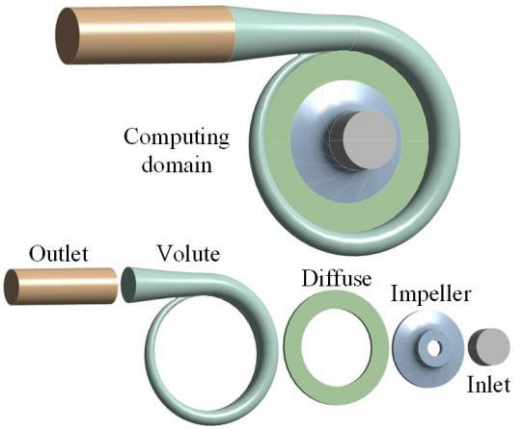

Fig. 2 Flow channel model of the centrifugal air compressor

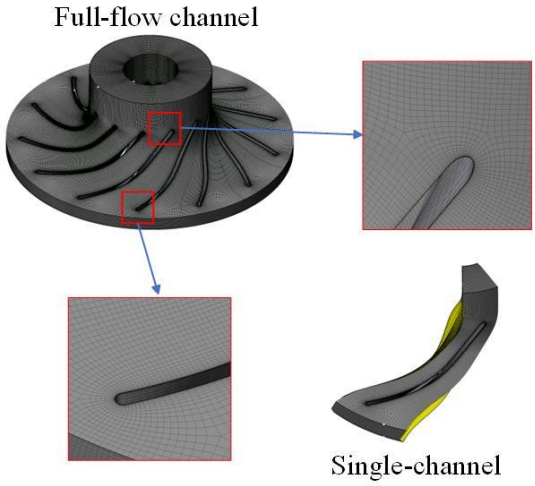

Fig. 3 Mesh generation of impeller

Table 1 Impeller structural parameters

Parameters	Value
Impeller outlet diameter D_2	74
Impeller inlet diameter D_1	36
Hub diameter D_h	16
Outlet width b_1	4
Number of blades Z	13
Outlet blade angle β_{2A}	40
Inlet blade angle β_{1A}	50

The mass flow rate of the compressor was determined by the output power, and the theoretical mass flow rate for the compressor design was calculated using the following formula (Liu et al., 2022):

$$Q_m = 3.58\times10^{-4}\times\lambda\times\frac{P_e}{V_c}(\text{kg/s}) \tag{7}$$

The stoichiometric ratio of air in the fuel cell stacks was typically maintained at 2.2 (Cunninghan et al., 2001). For commercially-available fuel cell passenger vehicles with a stack power of 60 kW (Liu et al., 2022), the average cell voltage is generally set to 0.6 V. Calculations yielded an airflow requirement of approximately 0.08 kg/s. However, considering the inevitable air leakage in pneumatic systems, the design mass flow rate of the centrifugal air compressor was conservatively determined as 0.09 kg/s. Figure 2 shows the three-dimensional structure of the impeller and Table 1 lists the main structural parameters of the impeller after the preliminary design.

2.3 Boundary Conditions

The meshing workflow for the compressor components was performed using TurboGrid and ANSYS meshes. An all-hexahedral structured mesh was employed for the impeller domain to resolve the high-speed rotational flow characteristics and ensure grid orthogonality. Unstructured tetrahedral meshing was applied to the stationary components to ensure geometric adaptability. Boundary layer meshing with $y^+ < 10$ was incorporated to resolve the near-wall flow physics. The mesh interfaces between the rotating and stationary domains were configured using a grid interface to maintain flux conservation. ANSYS FLUENT was used as the CFD solver. To save time and improve efficiency, a one-thirteenth single-channel mesh division was used as the optimization objective for all meshes, as shown in Fig. 3.

Table 2 Verification of grid independence for compressors

Grid number	Pressure ratio	Isentropic efficiency
152682	1.87	90.4%
398454	1.98	91.14%
508097	2.06	92.06%
537807	2.13	92.14%
578804	2.14	92.7%
636619	2.24	94.15%
729708	2.25	94.15%

When performing fluid simulations for rotating machinery, FLUENT provides a calculation method called the multiple reference frame (MRF) method. This method rotates the coordinate system and directly sets the rotational speed for the moving mesh, thereby transforming the transient model into a steady-state model for the solution. The turbulence model adopts the SST k-ω. The boundary condition at the inlet was a pressure inlet, with the total pressure of the inlet set to atmospheric pressure and the inlet temperature set to 293 K. The boundary condition at the outlet was a mass-flow outlet having a magnitude of 0.0074 kg/s. The wall surface that rotates with the rotating area was defined as a moving wall, with the movement mode set to rotation and its speed defined as 100,000 rpm. The solver selected the pressure-velocity coupling method, using a second-order upwind format for the pressure, density, kinetic energy, and turbulent energy.

2.4 Grid Independent Study

The number of mesh cells significantly affects the simulation time as well as accuracy, thus making it crucial to strike a balance between their excessive and insufficient

Table 3 Comparison of numerical and experimental data

mass flow rate	Performance	Exp. value	Sim. value	Error
6.09 kg/s	Pr	2.061	1.999	3.01%
	Ie	86.8%	88.3%	1.73%
5.31 kg/s	Pr	2.094	2.071	1.1%
	Ie	88.0%	90.1%	2.39%
4.53 kg/s	Pr	2.086	2.157	4.65%
	Ie	86.5%	90.2%	4.28%

amount. In this study, a single-channel model with mass flow rate of 0.0074 kg/s was considered for verifying the mesh independence. Table 2 presents the pressure ratio for each the outlet total pressure of the impeller calculated using different cell numbers while keeping the boundary conditions consistent. It is evident that utilizing 636,619 cells not only meets the accuracy requirements but also reduces the computational time.

2.5 Numerical Validation

To validate the fidelity of the numerical simulations in this study, the benchmark Eckardt impeller was analyzed under identical boundary conditions (SST k-ω turbulence model, rotational speed: 14,000 rpm) (Eckardt, 1976). A rigorous comparison between the simulated performance characteristics at the design speed and experimental data for the Eckardt impeller, obtained from (Liu & Wang, 2019; Eckardt, 1975), is presented in Fig. 4 and Table 3. The results demonstrate that despite minor pressure ratio fluctuations across varying mass flow rates, the total pressure ratio deviation as well as the isentropic efficiency discrepancy remain within the 5 % thresholds. This confirms that the numerical methodology achieved engineering-grade accuracy, effectively substituting physical experiments for preliminary design evaluations. Therefore, the numerical calculation method used in this study is sufficiently accurate and can be used to provide accurate predictions for the compressor.

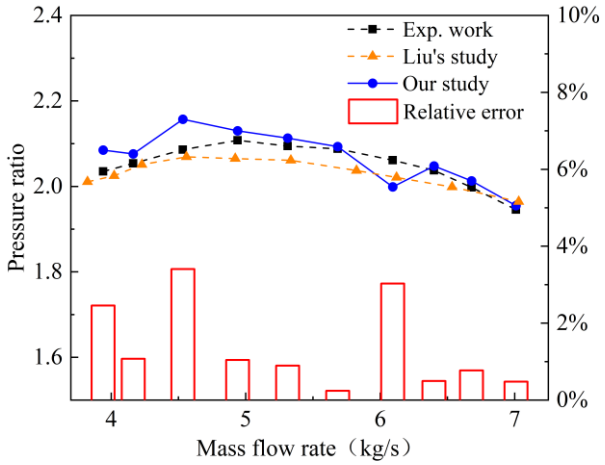

Fig. 4 Numerical verification of the compressor in this study

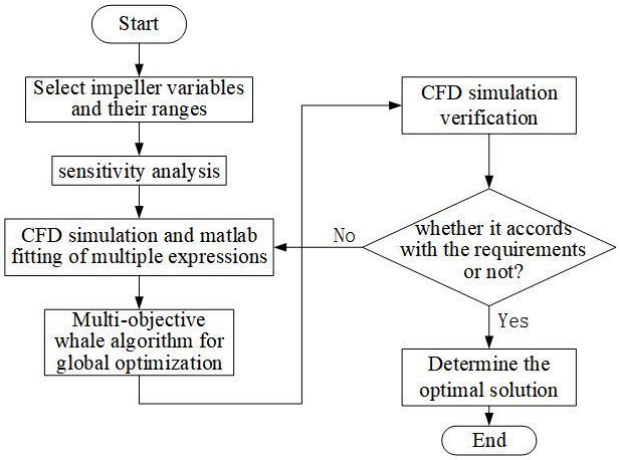

Fig. 5 Multi-objective optimization flow chart of compressor impeller

3. Multiparameter and Multi-objective Optimization for the Impeller

3.1 Construction of the Optimization Problem and Sensitivity Analysis

The pressure ratio (*Pr*) and isentropic efficiency (*Ie*) are the two crucial performance parameters of compressors, which are the optimization objectives of this study. The formulae are as follows:

$$\varepsilon = \frac{P_{2t}}{P_{1t}} \tag{8}$$

$$\eta = \frac{\left(\frac{P_2}{P1}\right)^{\frac{k-1}{k}} - 1}{\frac{T_2}{T_1} - 1} \tag{9}$$

The optimized process is shown in Fig. 5. The specific multi-objective and multi-operating-condition optimization processes are as follows.

(1) Determination of the structural parameters of the impeller and its optimization objectives: Six variables, including the inlet angle (β_{1A}), outlet angle (β_{2A}), outlet width (b_1), blade thickness (S), outlet radius (R_2), and number of blades (Z), were selected as the initial design parameters for the impeller. The optimization objectives chosen corresponded to the aerodynamic performance of the impeller, namely, the *Pr* and *Ie*.

(2) Sensitivity analysis of the design parameters: LHS was used for selecting the experimental samples. CFD simulations were performed to obtain the *Pr* and *Ie* of each sample. The correlation coefficients of each design parameter were calculated to identify the parameters that

significantly affected the aerodynamic performance of the impeller, thereby reducing the complexity of the subsequent optimization.

(3) Fitting of approximation models: Different weights were assigned to the rated and typical operating conditions based on the air supply requirements of the fuel cell vehicles. A mathematical model for the total pressure ratio and efficiency was derived by applying least-squares regression analysis to fit the mathematical surrogate model of the optimization objectives of the impeller, which served as the objective functions for this optimization.

(4) Multi-objective optimization: A multi-objective WOA was employed to obtain the optimal solution set for the objective functions. The technique for order preference by similarity to ideal solution (TOPSIS) method was used for decision-making to determine the optimal solution. The accuracy of the results was verified using CFD simulations.

In this study, with the *Pr* and *Ie* as the optimization objectives, the inlet angle, outlet angle, outlet width, blade thickness, outlet radius, and blade number were initially selected as the optimization variables.

In terms of the gas supply requirements of fuel cell vehicles, two typical operating conditions, namely, rated and typical operating conditions, of the air compressor were studied. When the vehicle accelerates, the fuel cell requires a high-power output, thus requiring a large output pressure ratio under rated conditions. When the vehicle travels at a constant speed, efficiency is very important. Thus, the efficiency under typical operating conditions should be higher. Different weights were set based on the acceleration performance requirements of fuel cell vehicles and typical operating conditions. The pressure ratio under high-load conditions of the fuel-cell stack requires a large inlet mass flow rate and pressure ratio. However, the desired efficiency under the economic conditions of a small intake mass flow should be as high as possible. The weights for the pressure ratio in the rated and typical operating conditions were set to 0.7 and 0.3, respectively, whereas the proportions of efficiency in these conditions were set to 0.3 and 0.7, respectively. The centrifugal air compressor was then optimized considering multiple objectives and operating conditions. The pressure ratio and efficiency for each condition can be expressed as:

$$\begin{cases} \varepsilon_e = A_1\left(\beta_{1A},\beta_{2A},b_1,s,R_2,Z\right) \\ \varepsilon_c = A_2\left(\beta_{1A},\beta_{2A},b_1,s,R_2,Z\right) \\ \eta_e = B_1\left(\beta_{1A},\beta_{2A},b_1,s,R_2,Z\right) \\ \eta_c = B_2\left(\beta_{1A},\beta_{2A},b_1,s,R_2,Z\right) \end{cases} \tag{10}$$

Where, $\varepsilon_e$is the objective function of the *Pr* under rated operating conditions, ε_c is the objective function of the *Pr* under typical operating conditions, η_e is the entropic efficiency objective function under rated operating conditions, and η_c is the entropic efficiency objective function under typical operating conditions.

The weighted objective function is:

Table 4 Design variable range

Types	Number range
β_{1A} /°	40~60
β_{2A} /°	30~50
b /mm	3~5
s/mm	1~3
R_2 /mm	34~41
Z	11~15

$$Max\begin{cases} \varepsilon = 0.7\varepsilon_e + 0.3\varepsilon_c \\ \eta = 0.3\eta_e + 0.7\eta_c \end{cases} \tag{11}$$

The optimization involved selecting six structural parameters that influence the performance of the impeller. Considering the significant sample space that would result from including all six parameters in the optimization, a sensitivity analysis was conducted before optimization to determine the degree of influence of each structural parameter on the aerodynamic performance of the compressor. Parameters with relatively small effects on the performance were eliminated. Table 4 lists the ranges of the design variables.

Based on the *Pr* and *Ie*, an LHS experimental design with a sample size of 50 was established. Numerical simulations were performed for each sample point to obtain the aerodynamic performance of the impeller under the two operating conditions. The correlation coefficients between the aerodynamic performance of the impeller and the various parameters under the rated and typical operating conditions are shown in Fig. 6.

By weighting the aerodynamic performance and correlation coefficients of the various parameters for the rated and typical operating conditions, it was determined that the influence of the structural parameters on the *Pr* and *Ie* decreased in the following order: outlet radius, blade thickness, inlet angle, outlet width, outlet angle, and number of blades. Accordingly, the outlet radius, blade thickness, inlet angle, and outlet width were selected as the optimization variables, and a multi-objective optimization problem was formulated as follows:

$$\begin{cases} \mathrm{Max}\left(\varepsilon,\eta\right) \\ \varepsilon = A\left(R_2,s,\beta_{1A},b_1\right) \\ \eta = B\left(R_2,s,\beta_{1A},b_1\right) \\ \text{s.t. } R_2 \in \left[34,41\right] \\ s \in \left[1,3\right] \\ \beta_{1A} \in \left[40,60\right] \\ b_1 \in \left[3,5\right] \end{cases} \tag{12}$$

3.2 Approximate Model Fitting and Verification

In this study, least-squares regression analysis was done for polynomial fitting, and a four-element second-order response surface function was used as follows (Esfe et al., 2022):

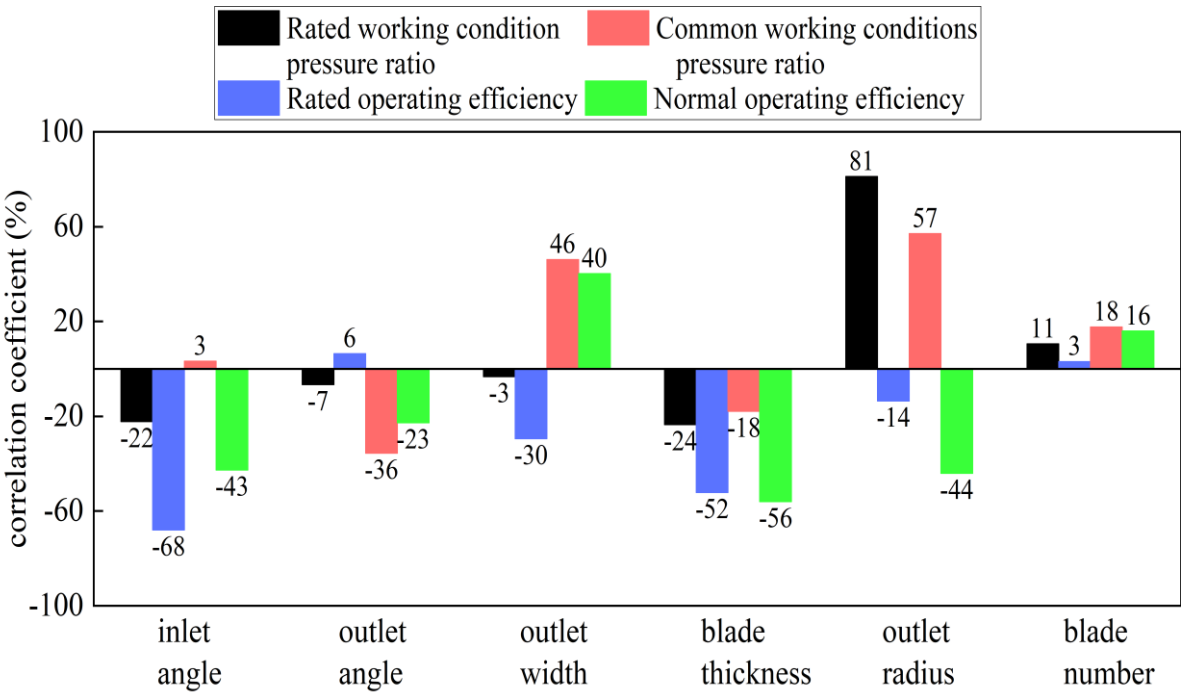

Fig. 6 Correlation coefficient between variables and aerodynamic performance under two operating conditions

Table 5 Latin hypercube sample after sensitivity analysis

Number	R_2 /mm	S /mm	β_{1A} /°	b_1 /mm	ε_e	η_e	ε_c	η_c
1	35.96	2.17	56.92	4.84	2.1439	0.8942	1.3480	0.9350
2	34.26	1.56	47.20	4.55	2.1836	0.9501	1.3314	0.9518
3	37.19	1.17	50.49	3.42	2.2804	0.9503	1.3393	0.9449
4	38.38	1.95	54.03	4.97	2.2503	0.8983	1.3719	0.9379
5	36.37	2.95	59.20	3.04	2.0728	0.8850	1.2912	0.8989
…	…	…	…	…	…	…	…	…
46	39.35	2.74	40.94	4.28	2.3463	0.9304	1.3640	0.9336
47	34.57	2.60	46.56	4.89	2.0980	0.9092	1.3320	0.9432
48	39.11	2.77	55.80	4.36	2.2052	0.8769	1.3612	0.9255
49	38.92	1.78	42.17	4.18	2.3611	0.9426	1.3668	0.9424
50	37.06	1.90	45.83	4.68	2.2768	0.9241	1.3635	0.9477

$$Y = \beta_0 + \sum_{i=1}^{4} \beta_i x_i + \sum_{i=1}^{4} \beta_{ii} x_i^{\,2} + \sum_{i=1}^{4} \beta_{ij} x_i x_j + a \tag{13}$$

where β_0, β_i, β_{ii}, and β_{ij} symbolize the regression coefficients, x_i and x_j represent variables, and a is the fitting error.

The experimental samples resampled with the four optimization variables are shown in Table 5 as the LHS samples of the four variables after sensitivity analysis.

Parametric interaction between control factors and the response value was fitted using MATLAB programming. The pressure ratios under the rated and typical operating conditions, and the isentropic efficiencies were weighted. The fitting relationship between each structural parameter, *Pr*, and *Ie* was obtained as follows:

$$\begin{aligned}\varepsilon = {} & 0.7*(-6.2364+0.2413R_2+0.3268s+0.0614\beta_{1A} \\ & +0.8430b_1-0.0009R_2s-0.0007R_2\beta_{1A}-0.0077R_2b_1 \\ & -0.0029s\beta_{1A}-0.0353sb_1-0.0026\beta_{1A}b_1-0.0018R_2^2 \\ & -0.0176s^2-0.0002\beta_{1A}^2-0.0446b_1^2) \\ & +0.3*(-0.1029+0.0562R_2-0.0172s+0.0025\beta_{1A} \\ & +0.0869b_1+0.0002R_2s-0.0001R_2b_1+0.0021sb_1 \\ & -0.0007R_2^2-0.0018s^2-0.0087b_1^2)\end{aligned} \tag{14}$$

$$\begin{aligned}\eta = {} & 0.3*(-0.4978+0.0087R_2+0.1271s+0.0311\beta_{1A} \\ & +0.2593b_1-0.0005R_2s-0.0004R_2\beta_{1A}-0.0039R_2b_1 \\ & -0.0013s\beta_{1A}-0.0128sb_1-0.0006\beta_{1A}b_1+0.0003R_2^2 \\ & -0.0044s^2-0.0001\beta_{1A}^2-0.0095b_1^2) \\ & +0.7*(0.5755+0.0072R_2-0.0033s+0.0084\beta_{1A} \\ & +0.035b_1+0.0004R_2b_1-0.0002s\beta_{1A}+0.0023sb_1 \\ & -0.0001R_2^2-0.0016s^2-0.0001\beta_{1A}^2-0.0058b_1^2)\end{aligned} \tag{15}$$

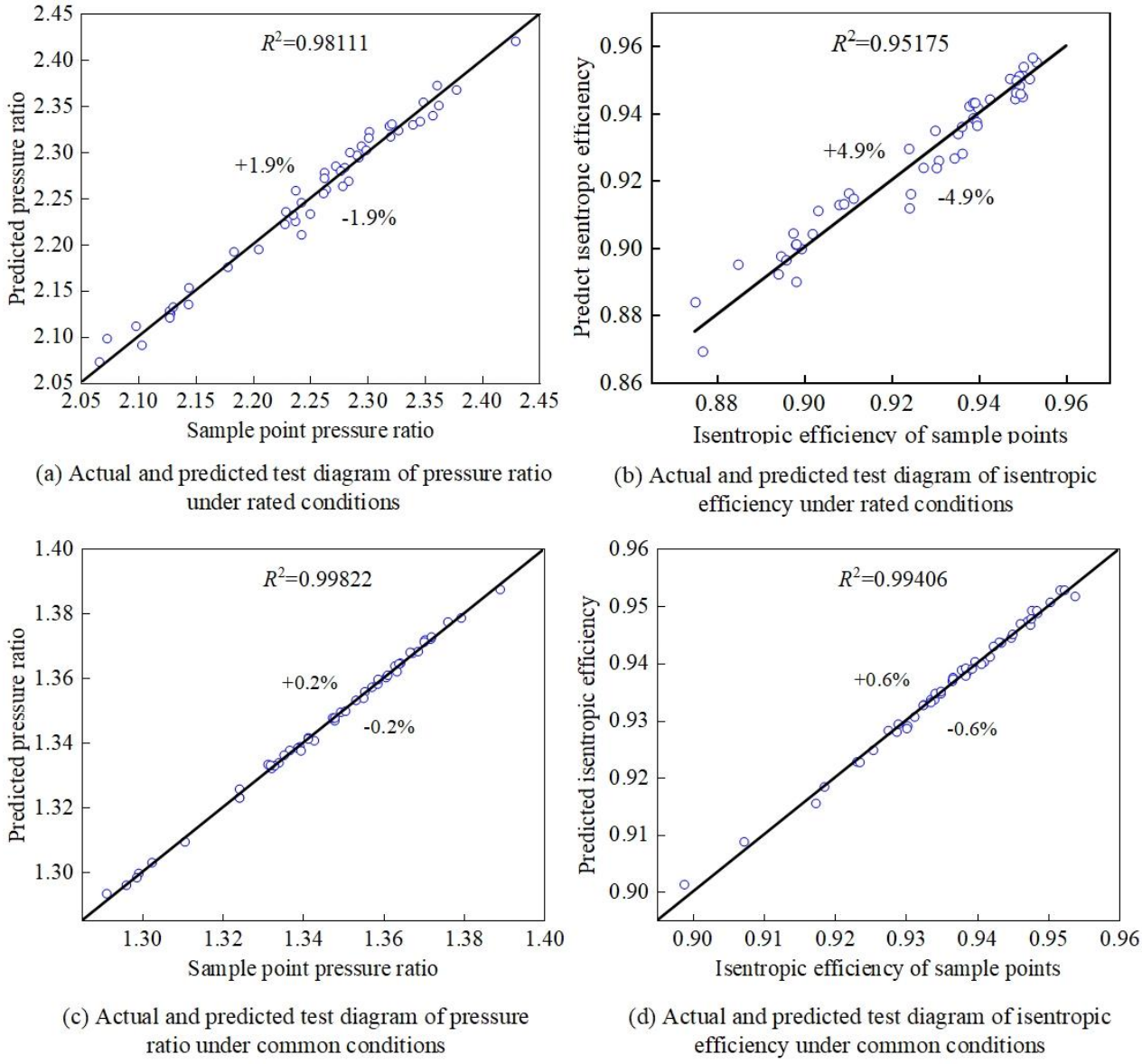

Fig. 7 Verification chart of response values and predicted responses under rated and common conditions

After fitting, the accuracy of the fitting model was tested using the coefficient of determination, R^2 (Ma et al., 2022) using the following expression:

$$R^2 = 1-\frac{\sum_{i=1}^{n}(y_i-y)^2}{\sum_{i=1}^{n}(y_i-\bar{y})^2} \tag{16}$$

where $\hat{y}$ is the *Pr* or *Ie* predicted by the model, $\bar{y}$ represents the average value predicted by the model, and y_i is the *Pr* or *Ie* of the i_{th} sample point.

Figures 7 show test graphs of the optimization objectives and predictive optimization objectives under the two working conditions. A higher concentration of points near the line with a slope of 1 indicates better model accuracy. The R^2 values for the *Pr* and *Ie* under rated operating conditions were 0.98111 and 0.95175, respectively, whereas the corresponding values under typical operating conditions were 0.99822 and 0.99406, respectively, which are close to 1. The relative errors were constrained to below 1.9, 4.9, 0.2, and 0.6 %, respectively, demonstrating subpercentage-level accuracy across all measured parameters and indicating a good degree of fitting.

3.3 Realization of Multi-condition and Multiparameter Optimization

The whale optimization algorithm (WOA) is inspired by the foraging behavior of humpback whales, where each solution candidate corresponds to a spatial position of the whale within the search space (Mirjalili & Lewis, 2016). The algorithm is mathematically formalized into three distinct phases: prey encircling, bubble-net attacking strategy, and global exploration for prey (Islam et al., 2021).

(1) Surround the prey

$$B = \left|E\vec{X}^{*}(t) - \vec{X}(t)\right| \tag{17}$$

$$\vec{X}(t+1) = \vec{X}^{\square}(t) - AB \tag{18}$$

Where, t represents the current iteration number; B is the distance between the whale and its prey; A, E are the coefficients; $\vec{X}^{\cdot}(t)$ is the best current position vector of the whale. $\vec{X}(t)$ is the current position vector of the whale.

(2) Hunting for prey

The hunting behavior of whales is a spiral movement, and its mathematical function is as follows:

$$\vec{X}(t+1) = \vec{X}^{*}(t) + \mathrm{B}e^{df}\ cos(2\pi l) \tag{19}$$

Where, d represents constant, defines the shape of the spiral line; f is random number, with a range from -1 to 1.

During whales' hunting process, both encircling and hunting behaviors are executed concurrently, with both behaviors assigned equal probabilities of 0.5. Let p denote a random number within the interval [0,1]. The mathematical function is as follows:

$$\vec{X}(t+1) = \begin{cases} \vec{X}^{*}(t) - AB, & p < 0.5 \\ \vec{X}^{*}(t) + \mathrm{B}_{p}e^{bl}\cos(2\pi l), & p > 0.5 \end{cases} \tag{20}$$

(3) Search for prey

$$B = \left|C\vec{X}_{\mathrm{rand}} - \vec{X}(t)\right| \tag{21}$$

$$\vec{X}(t+1) = \vec{X}_{\mathrm{rand}} - AB \tag{22}$$

where, X_{rand} is random position vector of the whale's location.

This study employed the WOA for parameter optimization and introduced nondominated sorting and crowding distance calculation to achieve multi-objective optimization (Jangir & Jangir, 2017). This method not only has low computational requirements but also steadily improves the quality of solutions in the population during iterations, leading to a better Pareto optimal solution set. Fig. 8 illustrates the optimization process of the multi-objective WOA.

To validate the superiority of the optimization algorithm used in this study, a comparison was made with the widely used nondominated sorting genetic algorithm II (NSGA-II) in the multi-objective domain. Global optimization was performed for the multi-objective expressions of the two optimization objectives to obtain the optimal solution sets, from which the best solutions were selected. To ensure fairness, both algorithms were set to an initial population of 150 and a maximum iteration count of 200. Figure 9 shows the Pareto-optimal solution sets obtained using the two algorithms.

As illustrated in Fig. 9, the red markers denote the Pareto-optimal solutions obtained by NSGA-II, whereas the black markers represent the nondominated solutions generated by the proposed nondominated sorting whale optimization algorithm (NAWOA). The NAWOA solutions exhibit tighter clustering within the objective space while simultaneously achieving elevated pressure ratios and superior isentropic efficiencies. Therefore, it is evident that the Pareto solution set obtained using NAWOA is superior for the pressure ratio and isentropic efficiency functions. This algorithm demonstrates the advantages of multi-objective optimization problems for impeller optimization.

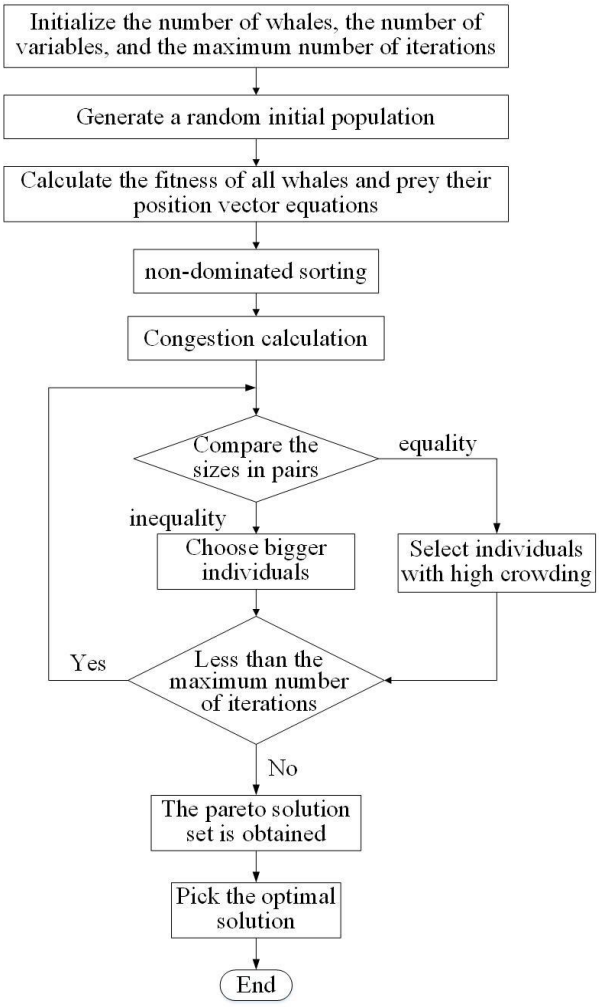

Fig. 8 Multi-objective whale algorithm optimization process

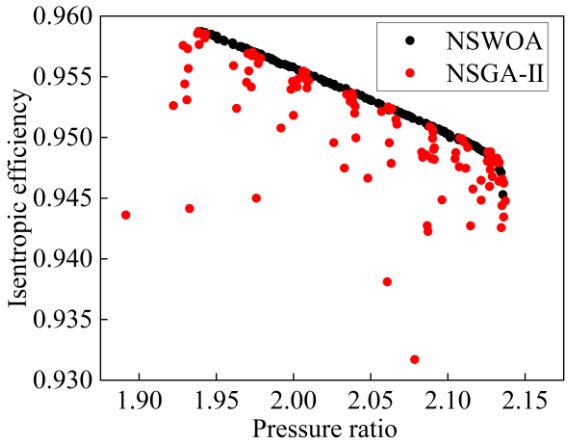

Fig. 9 Comparison of performance between two algorithms

Table 6 Ranking top ten solutions in the optimal solution set obtained through evaluation

Number	Design variable				Optimization objective		Optimal level index
	R_2 /mm	s/mm	β_{1A} /°	b_1 /mm	Weight pressure ratio	Weighting efficiency	
1	39.62	1.01	45.33	4.12	2.1005	0.9503	0.81610
2	39.62	1.01	45.33	4.07	2.0994	0.9503	0.81064
3	39.57	1.02	45.21	4.08	2.0987	0.9503	0.80699
4	39.56	1.01	46.26	4.14	2.0984	0.9504	0.80586
5	39.60	1.01	45.35	4.03	2.0983	0.9504	0.80512
6	39.48	1.01	45.61	4.14	2.0975	0.9505	0.80150
7	39.47	1.01	45.47	4.08	2.0961	0.9505	0.79421
8	39.51	1.01	45.59	4.03	2.0960	0.9505	0.79382
9	39.37	1.01	45.59	4.17	2.0955	0.9506	0.79158
10	39.34	1.01	45.59	4.17	2.0948	0.9506	0.78815

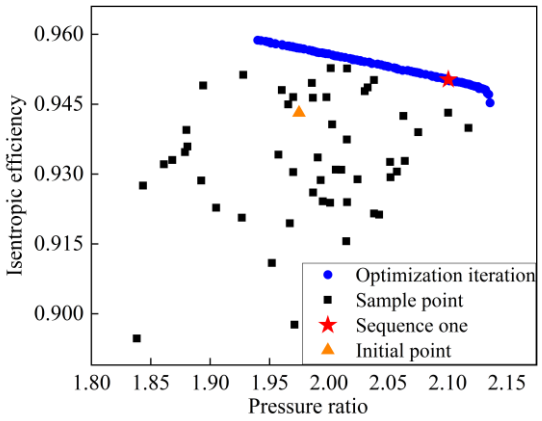

Fig. 10 Schematic diagram of the position of sequence 1 before optimization, sample points, and optimal solution set

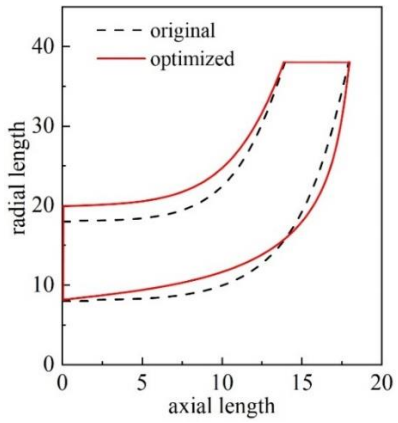

Fig. 11 Comparison of the impeller's meridional surface before and after optimization

3.4 Goal Decision

Using the *Pr* and *Ie* of the impeller as indicators, the optimal solution set obtained by the NSWOA was processed by introducing the ordered weighted averaging (COWA) operator to calculate the objective weights of the two performance indicators (Tang & Yang, 2018). The optimal solution set was then weighted, and the TOPSIS method was employed to calculate the proximity index of each point to the optimal level.

The solutions were ranked accordingly, and the top 10 solutions in the optimal solution set are listed in Table 6.

Finally, the solution ranked first was selected as the optimal design choice in the impeller's multi-objective optimization. Figure 10 shows a schematic diagram of the position of this solution before optimization, the sample points, and their location in the optimal solution set.

As shown in Table 7 and Fig. 10, under the rated operating conditions, the *Pr* and *Ie* of the optimal scheme are, respectively, 6.3 and 0.9 % higher than those of the initial scheme, respectively. Under typical operating conditions, the *Pr* and *Ie* are 2.7 and 1.7 %, respectively, which proves that the method of multi-objective optimization for compressor impeller combine with multi-working conditions is effective and feasible.

Table 7 Comparison results between the best solution and the initial solution

Parameter	Before optimization	Optimization
R_2/mm	37	39.62
s/mm	2	1.01
β_{1A} /°	50	45.33
b_1/mm	4	4.12
ε_e	2.2474	2.389
η_e/%	94.1575	94.992
ε_c	1.3389	1.3749
η_c/%	94.385	96.016

4. COMPARISON OF THE SIMULATION RESULTS

(1) Single-channel Pressure Comparison

Figure 12 exhibits the axial pressure distribution of the impeller before and after optimization under the two operating conditions. It can be observed that the outlet static pressure of the impeller increased from 216 to 229 kPa for the rated operating condition and from 132 to 135 kPa for the typical operating condition after optimization. This indicates an improvement in the pressure ratio in both types of conditions after optimization.

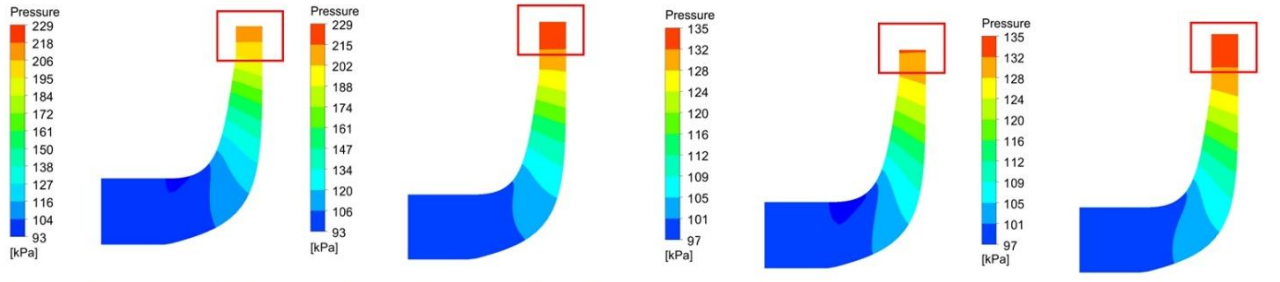

(a) Pressure distribution under rated conditions before optimization

(b) Pressure distribution under rated conditions after optimization

(c) Pressure distribution under common conditions before optimization

(d) Pressure distribution under common conditions after optimization

Fig. 12 Comparison of pressure map on the radial surface of the impeller under two operating conditions

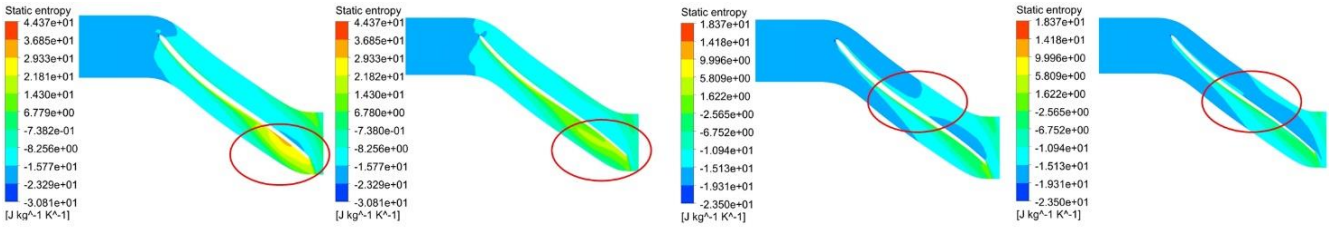

(a) Static entropy distribution of 80% blade height under rated condition before optimization

(b) Static entropy distribution of 80% blade height under rated condition after optimization

(c) Static entropy distribution of 80% blade height under common before optimization

(d) Static entropy distribution of 80% blade height under common after optimization

Fig. 13 Comparison of static entropy distribution for impeller flow channels with 80% blade height under two operating conditions

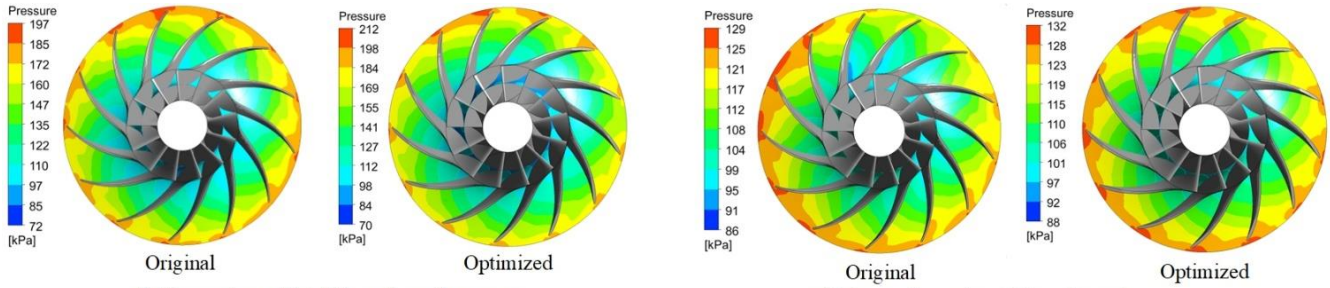

(a)Comparison of total flow channel pressure under design conditions

(b)Comparison of total flow channel pressure under common conditions

Fig. 14 Comparison of pressure for the full-flow section with 50% blade height under two operating conditions

(2) Single-channel Entropy Comparison

Based on the concept of entropy proposed by Clausius, entropy generation caused by irreversible processes, such as friction and flow separation during compression, leads to thermodynamic losses. In this study, static entropy refers to the specific entropy (entropy per unit mass), which is defined as (Nakonieczny, 2002):

$$E = c_p \ln(T_2 / T_1) - R \ln(P_2 / P_1) \tag{23}$$

where R denotes the air constant and c_p represents the specific heat at constant pressure. Figure 13 illustrates the static entropy generation analysis at 80 % blade height of the impeller under the two operating conditions before and after optimization. A higher static entropy indicates greater turbulence and flow losses, resulting in a lower efficiency. The maximum static entropy decreased from 44.73 to 42.72 J/kgK for the rated operating condition and from 43.63 to 10.86 J/kgK for the typical operating condition after optimization. The reduction in the static entropy at the outlet indicates optimization of the flow field within the impeller, leading to improved efficiency.

(3) Full-flow Passage Pressure Analysis

Aerodynamic analysis in Figure14 quantifies spanwise pressure gradient evolution (z/h=0.5) through compressor blade passages pre- and post-optimization. The optimized impeller demonstrated a significantly higher outlet pressure than the baseline. Under the design conditions, the maximum outlet pressure increased from 197 (baseline) to 212 kPa (optimized). Under typical operating conditions, the outlet pressure increased from 129 (baseline) to 132 kPa (optimized). These results confirm

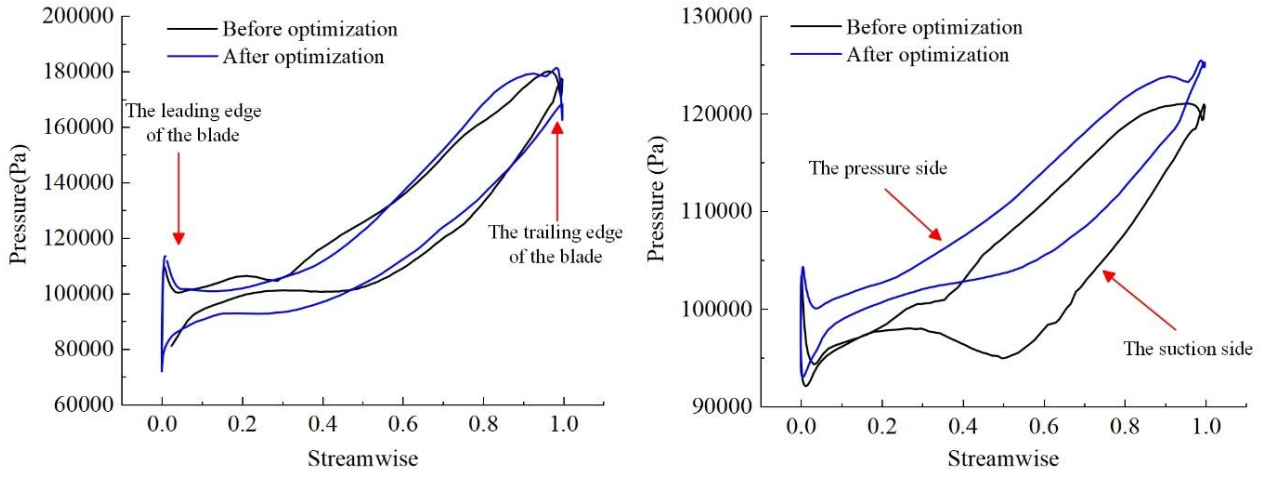

(a) Pressure distribution along the blade flow passage under rated condition

(b) Pressure distribution along the blade flow passage under common condition

Fig. 15 Comparison of pressure distribution along the blade flow passage under two operating conditions

that the pressurization capability of the impeller is significantly enhanced, whereas other losses are reduced.

(4) Static Pressure Distribution along the Blades

Figure 15 illustrates the static pressure distribution at 50 % span height for the blade flow passage. The optimized blade exhibited a smoother pressure profile with reduced fluctuations, particularly at higher pressure ratios near the trailing edge. The suction as well as the pressure sides of the optimized blade exhibited more uniform pressure gradients compared to the baseline. Consequently, the pressure-loading capacity and flow stability of the blade were improved.

(5) Comparison of the Optimization Results

Figure 16 presents a comparison of the optimization outcomes for five randomly selected operating conditions. Investigations into the mixed-flow dynamics of axial-flow pumps under five distinct operating conditions, along with analyses of blade angle effects, offer valuable insights for researchers and engineers. These findings facilitate a more comprehensive understanding of compressor dynamics under varying operating conditions (Al-Obaidi & Alhamid, 2023; Al-Obaidi et al., 2023), providing detailed and in-depth references for this study. As shown in the figure, the optimized impeller demonstrated improved performance in pressure ratio as well as isentropic efficiency across all five conditions. Specifically, the first condition corresponds to the typical operating condition mentioned earlier, with improvements of 3.6 % in the *Pr* and 4.1 % in the *Ie*. The fifth condition represents the design condition, in which the *Pr* and *Ie* increased by 5.5 and 1.4%, respectively. Overall, these results confirm that the performance of the centrifugal compressor was substantially enhanced by the optimization approach investigated in this study.

(6) Optimization effect comparison and uncertainty analysis of results

To fully demonstrate the novelty of this research and explicitly indicate the performance improvements achieved by the proposed optimization method, Table 8

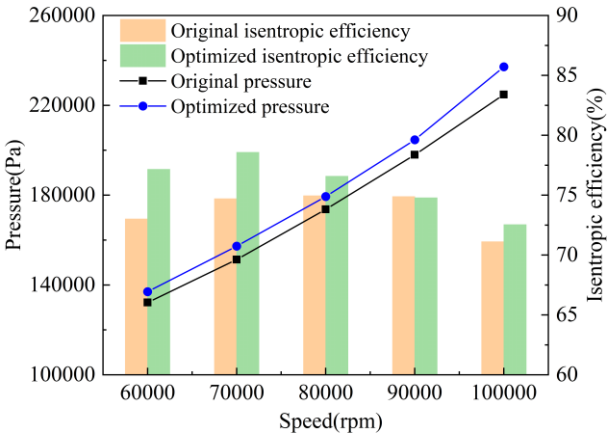

Fig. 16 Comparison of optimization outcomes for five randomly selected operating conditions

presents a comparison between the optimization results obtained in this study and those reported in relevant literature, where '–' indicates that the parameter was not included as an optimization objective. For collaborative optimization, Ekradi (Ekradi & Madadi, 2020) employed an ANN-NSGAII combined optimization method, achieving improvements of 0.74 and 0.97% respectively. Sun et al. (Sun et al., 2024) utilized a Stacking model integrated with GWO, attaining enhancements of 2.8 and 9.3% respectively; however, neither considered optimization for off-design conditions. For one-dimensional loss model analysis, Chen et al. (Chen et al., 2023) and Yuan et al. (Yuan et al., 2025) adopted different optimization algorithms. The former focused solely on improving isentropic efficiency, while the latter reported gains of 4.13 and 3.11%. Comparatively, this study not only achieves superior performance improvements under design conditions but also considers optimization across typical operating conditions, making the overall performance enhancement evident.

To analyze the uncertainty of the results, the structural parameters of the optimal solution obtained through optimization were input into the CFD simulation. Figure

Table 8 Optimization of the two working conditions in this study and the comparison with related research

Solution	Methods	Improvement	
		Pr	***Ie***
Ekradi	CFD + ANN + GA	0.74%	0.97%
Chen et al. (2023)	1-D loss model + GRG	-	1.24%
Sun et al. (2024)	CFD + Stacking model+ GWO	2.8%	9.3%
Yuan et al. (2025)	1-D loss model + SNR + GA	4.13%	3.11%
Design conditions of this study	CFD + LHS + NAWOA	**5.5%**	**1.4%**
Common conditions of this study	CFD + LHS + NAWOA	**3.6%**	**4.1%**

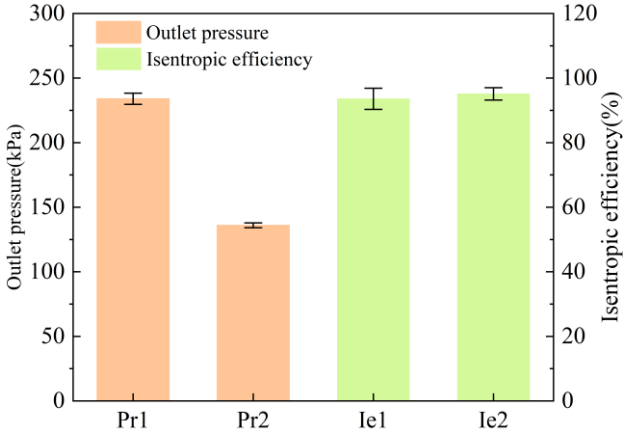

Fig. 17 Comparison of the simulated values and predicted values of the target structural parameters

17 explains the uncertainty analysis of the predicted values and the simulation values of the optimal solution. It is obvious that the relative error of the outlet pressure does not exceed 5%, and the isentropic efficiency does not exceed 4%, which proves the reliability of the prediction results.

5. CONCLUSION

In this study, a centrifugal compressor impeller was considered as the basis and the rated and typical operating conditions of fuel cell compressors were investigated. By assigning weights to the pressure ratio and efficiency under different operating conditions, these weighted values were set as the optimization objectives to conduct a multi-objective optimization of the compressor impeller. Some critical insights emerge from our study:

(1) A multi-objective optimization design method combining an approximation model, a WOA, and the TOPSIS decision-making method was adopted to realize a complete design process for optimizing the compressed performance and improvement in efficiency of a fuel cell compressor impeller.

(2) Using the pressure ratio and isentropic efficiency under rated and typical operating conditions as the optimization objectives and using the optimization variables screened through a sensitivity analysis based on LHS.

(3) The structural parameters that have the greatest impact on the performance of the impeller are outlet radius, maximum blade thickness, inlet angle, and outlet width.

(4) The determination coefficients R^2 of the fitting models are as follows: for the design conditions, they are 0.98 and 0.95; for the common conditions, they are 0.998 and 0.994. The relative errors are less than 1.9, 4.9, 0.2, and 0.6 %.

(5) Compared to the genetic algorithms, the Pareto solution set obtained by NAWOA was found to be superior for impeller optimization. By introducing the COWA operator and the TOPSIS decision-making method, the optimal solution set obtained by the NSWOA could be effectively ranked, enabling the rapid and efficient acquisition of the most suitable design results.

(6) Compared to the original compressor, the optimized single-channel impeller achieved a 5.5 % increase in the pressure ratio and a 1.4 % improvement in the isentropic efficiency under rated operating conditions, as well as a 3.6 % increase in the pressure ratio and a 4.1 % enhancement in the isentropic efficiency under typical operating conditions.

(7) Simulation results demonstrate that the optimized single-channel impeller achieves 5.9 and 1.04% increases in outlet static pressure at design and typical operating conditions, respectively.

(8) The optimized single-channel impeller exhibits significant reduction in static entropy at the outlet.

(9) The full-channel optimized impeller achieves outlet pressure improvements of 7.6 and 2.3%, demonstrating substantially enhanced pressure-boosting capability.

(10) Post-optimization, the pressure distribution curve along the impeller flow path becomes notably smoother with more uniform pressure distribution on both suction and pressure sides of blades.

(11) Quantitative analysis across five randomly selected operating conditions reveals improvements in pressure ratio and isentropic efficiency: 3.6% and 4.1%, 3.9% and 3.8%, 3.2% and 1.63%, 3.4% and -0.1%, 5.4% and 1.4% respectively.

(12) Uncertainty analysis confirms strong agreement between predicted and simulated results, with all errors remaining below 5%.

These findings provide crucial design principles for fuel cell compressor optimization and facilitate the implementation of fuel cell vehicles in practical

applications. Moreover, the optimization methodology developed in this study demonstrates strong generalizability. It is applicable not only to fuel cell compressors but also to compressors used in aerospace, marine, and industrial applications.

Limitations: The current study relies solely on CFD-based data simulation and lacks experimental verification. Furthermore, this investigation focused on optimization under design conditions and a single operational scenario. However, in real-world fuel cell electric vehicle operation, the mass flow rate and pressure ratio in a compressor varies dynamically, necessitating a comprehensive consideration of the full operating envelope of the fuel cell stack.

In future studies, the aforementioned results should be experimentally verified to validate the accuracy and efficacy of the optimization method. In addition, the investigations should focus on all operating conditions and remaining useful life of fuel cell air compressors, to promote the use of fuel cell vehicles and comprehensive multi-objective optimization.

CONFLICT OF INTEREST

Authors have no conflict of to disclose.

AUTHORS CONTRIBUTION

Y. Sun: Writing—Original Draft Preparation, Resources, Software, Validation, Visualization, Formal analysis; **W. Song**: Data-curation, Methodology; **H. Yin**: Resources, Methodology, Investigation, Supervision. **X. Sun**: Resources, Software. **A. Li**: Software. **Y. Chen**: Software.

REFERENCES

Abdullah, Z., Keeley, A. R., Coulibaly, T. Y., & Managi, S. (2024). The impact of fuel cell vehicles deployment on road transport greenhouse gas emissions through 2050: Evidence from 15 G20 countries. *Journal of Environmental Management*, *370*, 122660. https://doi.org/10.1016/j.jenvman.2024.122660

Abedin, T., Pasupuleti, J., Paw, J. K. S., Tak, Y. C., Mahmud, M., Abdullah, M. P., & Nur-E-Alam, M. (2025). Proton exchange membrane fuel cells in electric vehicles: Innovations, challenges, and pathways to sustainability. *Journal of Power Sources*, *640*, 236769. https://doi.org/10.1016/j.jpowsour.2025.236769

Al-Obaidi, A. R. (2023). Experimental diagnostic of cavitation flow in the centrifugal pump under various impeller speeds based on acoustic analysis method. *Archives of Acoustics*, *48(3)*, 159-170. https://doi.org/10.24425/aoa.2023.145234

Al-Obaidi, A. R. (2024a). Effect of different guide vane configurations on flow field investigation and performances of an axial pump based on CFD analysis and vibration investigation. *Experimental Techniques*, *48*, 69–88. https://doi.org/10.1007/s40799-023-00641-5

Al-Obaidi, A. R. (2024b). Evaluation and investigation of hydraulic performance characteristics in an axial pump based on CFD and acoustic analysis. *Processes*, *12(1)*, 129. https://doi.org/10.3390/pr12010129

Al-Obaidi, A. R., & Alhamid, J. (2023) Investigation of the main flow characteristics mechanism and flow dynamics within an axial flow pump based on different transient load conditions. *Iranian Journal of Science and Technology, Transactions of Mechanical Engineering 47*, 1397–1415. https://doi.org/10.1007/s40997-022-00586-x

Al-Obaidi, A. R., & Alhamid, J. (2024). Analysis of unsteady internal flow characteristics in axial pump with varying number of blades using computational modelling and vibration techniques. *Flow Measurement and Instrumentation*, *99*, 102654, ISSN 0955-5986. https://doi.org/10.1016/j.flowmeasinst.2024.102654

Al-Obaidi, A. R., & Alhamid, J. (2025). Experimental and simulation analyses of the hydraulic complex internal flow characteristics in an axial pump based on varying frequency vibration ranges technique. *International Journal on Interactive Design and Manufacturing (IJIDeM) 19*, 3661–3681. https://doi.org/10.1007/s12008-024-02012-9

Al-Obaidi, A. R., Alhamid, J., & Khalaf, H. (2024). Unsteady behaviour and plane blade angle configurations' effects on pressure fluctuations and internal flow analysis in axial flow pumps. *Alexandria Engineering Journal*, *99*, 83-107, ISSN 1110-0168. https://doi.org/10.1016/j.aej.2024.04.048

Al-Obaidi, A. R., Khalaf, H., & Alhamid, J. (2023, June). *Investigation of the influence of varying operation configurations on flow behaviors characteristics and hydraulic axial-flow pump performance.* Proceedings of the 4th International Conference on Science Education in The Industrial Revolution (Vol. 4).

Anbarsooz, M., Amiri, M., & Benini, E. (2024). A numerical investigation on the effects of vaned diffusers on the aerodynamic performance of a low pressure-ratio methane centrifugal compressor. *Journal of Applied Fluid Mechanics*, *17*(12), 2545-2562. https://doi:10.47176/jafm.17.12.2715

Boroujerdi, A., Simsek, Y., Bahri, P. A., & Urmee, T. (2025). Transitioning Australia's land freight transport: Competition of fuel cell electric, battery electric, and internal combustion engine vehicles, *Energy Conversion and Management*, *333*, 119798. https://doi.org/10.1016/j.enconman.2025.119798

Chen, Z., Huang, H., Chen, Q., Peng, X., & Feng, J. (2023). Novel multidisciplinary design and multi-objective optimization of centrifugal compressor used for hydrogen fuel cells. *International Journal of*

Hydrogen Energy, 12444-12460. https://doi.org/10.1016/j.ijhydene.2022.11.312

Cunningham, J. M., Hoffman, M. A., & Friedman, D. J. (2001). A Comparison of high-pressure and low-pressure operation of PEM fuel cell systems. *SAE Transactions*, *110*, 464–470. http://www.jstor.org/stable/44724322

Eckardt, D. (1975). Instantaneous measurements in the jet-wake discharge flow of a centrifugal compressor impeller. *Journal of Engineering for Gas Turbines & Power*, *97*(3), 337–345. https://doi.org/10.1115/1.3445999

Eckardt, D. (1976). Detailed flow investigations within a high-speed centrifugal compressor impeller. *Journal of Flu ids Engineering*, *98*(3), 390–399. https://doi.org/10.1115/1.3448334

Ekradi, K., & Madadi, A. (2020). Performance improvement of a transonic centrifugal compressor impeller with splitter blade by three-dimensional optimization. *Energy*, *201*. https://doi.org/10.1016/j.energy.2020.117582

Esfe, M. H., Motallebi, S. M., & Toghraie, D. (2022). Modeling and optimization of dynamic viscosity of oil-based nanofluids containing alumina particles and carbon nanotubes by response surface methodology (RSM). *Korean Journal of Chemical Engineering*, *39*(10), 2800-2809. https://doi.org/10.1007/s11814-022-1156-6

Guo, S., Duan, F., Tang, H., Lim, S., & Yip, M. (2014). Multi-objective optimization for centrifugal compressor of mini turbojet engine. *Aerospace Science and Technology*, *39*, 414-425, ISSN 1270-9638. https://doi.org/10.1016/j.ast.2014.04.014.

Hong, S., Mugabi, J., & Jeong, J. H. (2022). Numerical study on vortical flow structure and performance enhancement of centrifugal compressor impeller. *Applied Sciences*, *12*(15), 7755. https://doi.org/10.3390/app12157755

Islam, Q. N. U., Ahmed, A., & Abdullah, S. M. (2021). Optimized controller design for islanded microgrid using non-dominated sorting whale optimization algorithm (NSWOA). *Ain Shams Engineering Journal*, *12*(4), 3677-3689. https://doi.org/10.1016/j.asej.2021.01.035

Jangir, P., & Jangir, N. (2017). Non-dominated sorting whale optimization algorithm (NSWOA): a multi-objective optimization algorithm for solving engineering design problems. *Global Journals of Research in Engineering*, *17*(F4), 15-42. https://engineeringresearch.org/index.php/GJRE/article/view/1643

Li, X., Huang, N., Han, W., Tong, D., Zhang, Y., & Zhang, J. (2025). Numerical investigation of the impact of intake pipelines on the performance and flow characteristics of a centrifugal compressor. *Journal of Applied Fluid Mechanics*, *18(6)*, 1483-1501. https://doi.org/10.47176/jafm.18.6.3150

Liu, Y., Zhao, Y., Yang, Q., Liu, G., Li, L., & Gao, Z. (2022). Performance study of centrifugal air compressor for proton exchange membrane fuel cell systems. *Energy Science & Engineering*, *10*(1), 208-218. https://doi.org/10.1002/ese3.1023

Liu, Z., & Wang, S. (2019). Research on the stall signal recognition of centrifugal impeller by spatial fourier analysis. *Journal of Tianjin University (Science and Technology)*, *52*(4), 353-360.

Ma, C., Yang, Z., Jiao, K., Liu, Z., & Du, Q. (2021). Multi-objective optimization of the centrifugal compressor impeller in 130 kW PEMFC through coupling SVM with NSGA -III algorithms. *International Journal of Green Energy*, *18*(13), 1383–1395. https://doi.org/10.1080/15435075.2021.1904942

Ma, X., Chen, Z., & Zhao, Y. (2022). Optimal design of axially mixed excitation double salient pole aero-generator based on response surface method. *Aeronautical Science & Technology*, *33*(10), 74-81. https://doi:10.19452/j.issn1007-5453.2022.10.010.

Manzo, D., Thai, R., Le, H. T., & Venayagamoorthy, G. K. (2025). Fuel cell technology review: Types, economy, applications, and vehicle-to-grid scheme. *Sustainable Energy Technologies and Assessments*, *75*, 104229. https://doi.org/10.1016/j.seta.2025.104229

Mirjalili, S., & Lewis, A. (2016). The whale optimization algorithm. *Advances in Engineering Software*, *95*, 51-67. https://doi.org/10.1016/j.advengsoft.2016.01.008

Munson, B. R., Okiishi, T. H., Huebsch, W. W., & Rothmayer, A. P. (2013). *Fluid Mechanics* (pp. 271-274). Singapore: Wiley.

Nakonieczny, K. (2002). Entropy generation in a diesel engine turbocharging system. *Energy, 27*(11), 1027-1056. https://doi.org/10.1016/S0360-5442（02）00082-8

Niveditha, P., & Gopi, B. S. (2023). Effect of different types of external guide vanes on the performance of high-pressure centrifugal compressor. *Journal of Applied Fluid Mechanics*, *16(12)*, 2556-2568. https://doi.org/10.47176/jafm.16.12.1814

Soylemez, M. E., Behçet, R., & Parlak, Z. (2024). Analysis and optimization of the performances of the tandem blade radial compressor using the CFD. *Applied Sciences*, *14*(10), 4256. https://doi.org/10.3390/app14104256

Sun, X., Wang, H., Fu, J., Xia, Y., & Liu, J. (2024). Many-objective optimization for structural parameters of the fuel cell air compressor based on the Stacking model under multiple operating conditions. *Applied Thermal Engineering*, *245*, 122786, ISSN 1359-4311. https://doi.org/10.1016/j.applthermaleng.2024.122786

Tang, H., & Yang, S. (2018). Optimizing three-dimensional constrained ordered weighted averaging

aggregation problem with bounded variables. *Mathematics*, *6(9)*, 172. https://doi:10.3390/math6090172.

Wu, Y., Bao, H., Fu, J., Wang, X., & Liu, J. (2023). Review of recent developments in fuel cell centrifugal air compressor: Comprehensive performance and testing techniques. *International Journal of Hydrogen Energy*, *48(82)*, 32039-32055. https://doi.org/10.1016/j.ijhydene.2023.04.262

Yu, W., Sichuan, X., & Ni, H. (2015). Air compressors for fuel cell vehicles: An systematic review. *SAE International Journal of Alternative Powertrains*, *4*(1), 115-122. http://www.jstor.org/stable/26169070

Yuan, W., Lu, X., Qiu, Y., Zhang, Q., Yang, X., Wang, Y., & Zhang, L. (2025). Exploration of performance optimization strategies for micro-centrifugal compressors in hydrogen fuel cells: A synergistic analysis combining one-dimensional design and three-dimensional flow fields. *International Journal of Hydrogen Energy*, *131*, 229-244. https://doi.org/10.1016/j.ijhydene.2025.04.318

Zhang, Y., Chen, J., Shu, Y., Wang, Z., Yang, H., & Wei, Y. (2024). Effects of inlet tip clearance on internal flow characteristic and aerodynamic performance of centrifugal compressor. *Journal of Applied Fluid Mechanics*, *18*(1), 274-289. https://doi:10.47176/jafm.18.1.2590